

Article

Representative Dynamic Accumulation of Hydrate-Bearing Sediments in Gas Chimney System since 30 Kyr BP in the QiongDongNan Area, Northern South China Sea

Jinan Guan ^{1,2,3} , Menghe Wang ^{1,2}, Wei Zhang ^{4,5,*} , Lihua Wan ², Matthias Haeckel ³  and Qi Wu ^{6,*}

¹ School of Energy Science and Engineering, University of Science and Technology of China, Hefei 230026, China; guanja@ms.giec.ac.cn (J.G.); wangmhe@mail.ustc.edu.cn (M.W.)

² CAS Key Laboratory of Gas Hydrate, Guangdong Provincial Key Laboratory of New and Renewable Energy Research and Development, Guangzhou Institute of Energy Conversion, Chinese Academy of Sciences, Guangzhou 510640, China; wanlh@ms.giec.ac.cn

³ GEOMAR Helmholtz Centre for Ocean Research Kiel, 24148 Kiel, Germany; mhaeckel@geomar.de

⁴ Sanya Institute of South China Sea Geology, Guangzhou Marine Geological Survey, China Geological Survey, Sanya 572024, China

⁵ National Engineering Research Center for Gas Hydrate Exploration and Development, Guangzhou 510075, China

⁶ Guangxi Key Laboratory of Geomechanics and Geotechnical Engineering, College of Civil Engineering, Guilin University of Technology, Guilin 541004, China

* Correspondence: zwgmgs@foxmail.com (W.Z.); giecwuqi@foxmail.com (Q.W.)

Abstract: A stratigraphic complex composed of mass transport deposits (MTDs), where the gas occurrence allows for the formation of a gas chimney and pipe structure, is identified based on seismic interpretation in the QiongDongNan area of the northern South China Sea. During the Fifth Gas Hydrate Drilling Expedition of the Guangzhou Marine Geological Survey, this type of complex morphology that has close interaction with local gas hydrate (GH) distribution was eventually confirmed. A flow-reaction model is built to explore the spatial–temporal matching evolution process of massive GH reservoirs since 30 kyr before the present (BP). Five time snapshots, including 30, 20, 10, and 5 kyr BP, as well as the present, have been selected to exhibit key strata-evolving information. The results of in situ tensile estimation imply fracturing emergence occurs mostly at 5 kyr BP. Six other environmental scenarios and three cases of paleo-hydrate existence have been compared. The results almost coincide with field GH distribution below the bottom MTD from drilling reports, and state layer fracturing behaviors always feed and probably propagate in shallow sediments. It can be concluded that this complex system with 10% pre-existing hydrates results in the exact distribution and occurrence in local fine-grained silty clay layers adjacent to upper MTDs.

Keywords: QiongDongNan slope area; methane hydrate-bearing sediments; gas chimney; mass transport deposit; evolution dynamics; fracturing criterion



Citation: Guan, J.; Wang, M.; Zhang, W.; Wan, L.; Haeckel, M.; Wu, Q. Representative Dynamic Accumulation of Hydrate-Bearing Sediments in Gas Chimney System since 30 Kyr BP in the QiongDongNan Area, Northern South China Sea. *J. Mar. Sci. Eng.* **2024**, *12*, 834. <https://doi.org/10.3390/jmse12050834>

Academic Editor: Anabela Oliveira

Received: 20 April 2024

Revised: 11 May 2024

Accepted: 13 May 2024

Published: 17 May 2024



Copyright: © 2024 by the authors. Licensee MDPI, Basel, Switzerland. This article is an open access article distributed under the terms and conditions of the Creative Commons Attribution (CC BY) license (<https://creativecommons.org/licenses/by/4.0/>).

1. Introduction

Gas hydrate (GH) is an ice-like nonstoichiometric crystalline solid formed of water and methane. Natural GH can be found on the seabed, in ocean sediments, in deep lake sediments, as well as in the permafrost regions. The amount of carbon potentially trapped in natural hydrate-bearing deposits may be between 3×10^{15} to 1×10^{16} m³, which makes them of major interest as a potential energy resource [1,2]. The presence and occurrence of GH in oceanic continental slope areas have attracted extensive attention and particular interest for the sake of energy potential, marine geohazards, and climate change issues [3,4].

A seismically imaged gas chimney is a type of stratigraphic sedimentary and hydraulic area where vertical seismic reflection profiles generally indicate that seafloor geological structures in this layer possess excellent transport capacity for upward gas-bearing fluids,

and also lots of methane gas is trapped in conduit pores [5–7]. It ordinarily extends several strata sequences, provides an effective aisle for functionally connecting deep hydrocarbon sources with the shallow bottom boundary of the local gas hydrate stability zone (HSZ), and conveys these multiphase fluids into the seafloor surface through affiliated pipe structures on many occasions [8,9]. Hovland and Sommerville (1985) reported the identification of gas-charged sediments and the characteristics of two natural gas seepages in the North Sea, which suggested a gas–liquid mixture fluid seepage caused the pockmark development [10]. After that, the impacts of seabed pockmarks associated with gas chimneys on offshore construction and gas hydrate occurrence have been extensively investigated by Hovland and collaborators [11,12]. In passive continental marginal slope regions, diverse deposition activities along the down-slope direction promote shear stress to exceed the shear strength and subsequently cause sedimentary failure, thus generating another laterally extended complicated structure of mass transport deposits (MTDs) [13,14].

Plentiful biogenic methane produced from shallow organic matter and thermogenic methane produced by deep source rocks cross together through a main gas chimney area and enter into shallow seabed deposits, contributing to the formation of complex structural seepage GH reservoirs in a suitable thermodynamic environment [15–17]. If the fluent pipe structure is disturbed or even stabbed across by MTDs, the upward flow of methane-bearing fluids is blocked by a sudden decrease in layer permeability and is thus inclined to stop and remain in local layers to form abundant GHs with various occurrence states. Subsequently, pore pressure below gradually increases, and hydraulic failure is likely to occur. Therefore, gas chimneys and local MTD systems play a key role in the dynamic migration, occurrence, and accumulation of GH reservoirs [18–20]. These activities are presumed to have occurred in many gas chimney–hydrate geological systems from time to time with geologic and environmental impacts [21].

Combining the visible distribution states of GH from the drilling core samples, we discovered that the accumulation type of GH reservoirs in the Qiongdongnan Basin (QDNB) area of the northwestern South China Sea (SCS) (Figure 1a), to some extent, is similar to other typical marine reservoirs, such as the Ulleung basin in South Korea and the Krishna-Godavari (KG) basin in India [22,23]. The GH system in the Qiongdongnan (QDN) area is deemed to have the same distribution and accumulation traits described above. Previous gas and oil resource exploration surveys have identified large-scale gas chimney morphotypes in the target sediments by analyzing high-resolution seismic sections. The large range of low-frequency chaotic seismic reflection area, which is obviously different from the surrounding stratigraphy, indicates the presence of abundant gas. The boundary of this chimney scope was confined by the termination of the blanking reflection. The instantaneous frequency and some of the internal events can clearly reveal the fluid pathway of gas chimney and pipe structure. Bottom simulating reflector (BSR) characteristics usually appear at the top of these shapes, and fluid leakage channels show a pull-up trace of seismic indications reaching the seafloor [24–26]. During the Fifth Gas Hydrate Drilling Expedition of the Guangzhou Marine Geological Survey (GMGS5) expedition, visible GH crystals recovered from drilling cores mainly show various features such as massive, laminates, nodules and veins massive, layers, nodules, and veins (sites W07, 08, and 09). GHs cement into fractured clay is the dominant phase in fine-grain silty sediments and have a concentrated distribution [27,28].

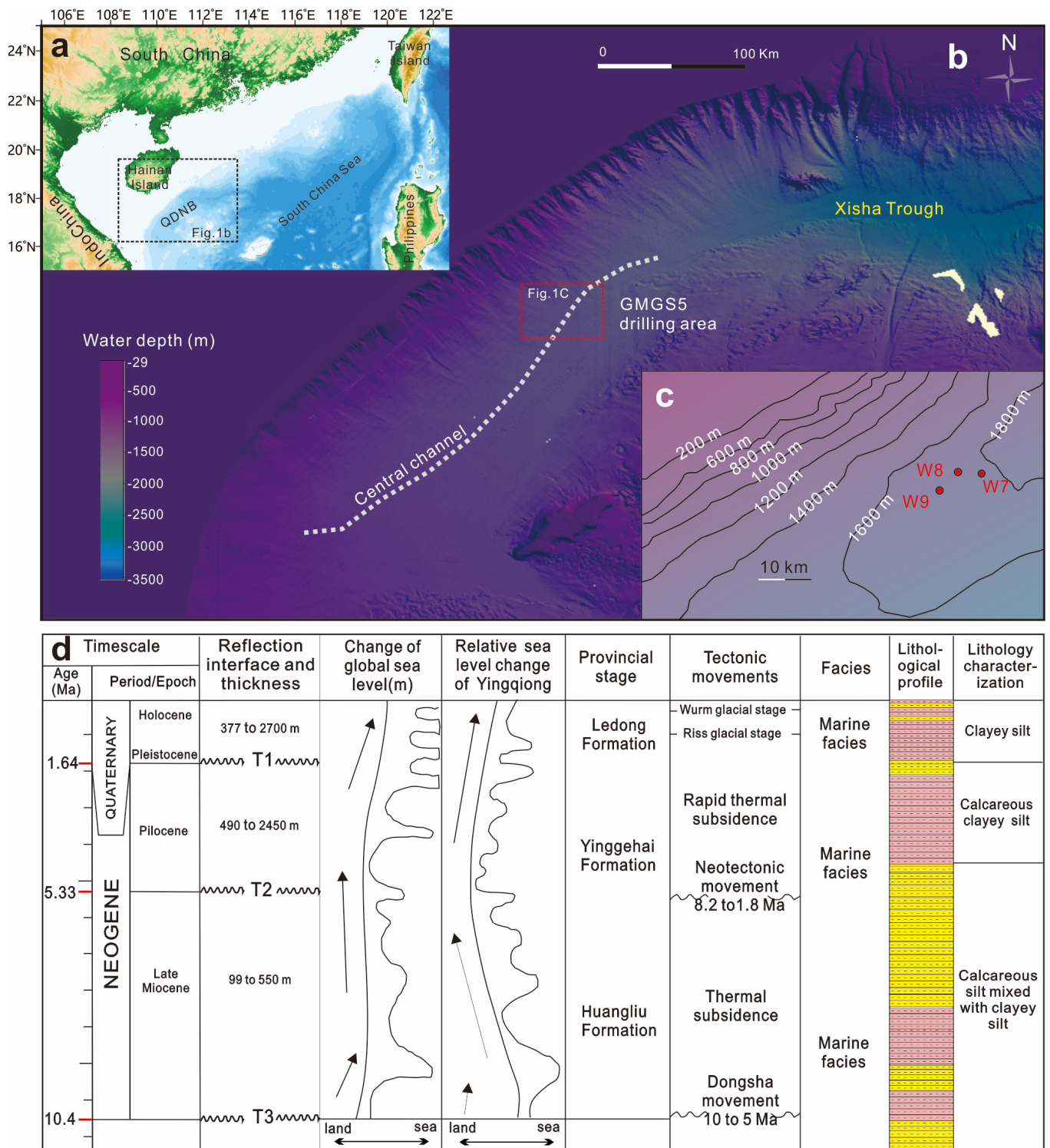


Figure 1. General geographic information and geological interpretation of the study area: (a) location of QDN area, (b) seafloor slope topography at GMSS5 drilling sites, (c) local seawater bathymetry contours, and (d) comprehensive stratigraphic histogram.

In recent years, remarkable progress has been made in understanding how local seismic chimneys and MTDs control fluid migration and determine the growth patterns of GH reservoirs from geologic, geochemical, and geophysical studies according to field investigation and the drilling core analysis results of GMGS5 [29,30]. In this study, we analyze GH reaction kinetics into the frame of a spatio-temporal dynamic evolution scale

in a well constrained geological background. We considered that the evolution process of GH reservoirs is also controlled by environmental factors such as seafloor deposition, eustatic sea-level change, and organic gas supply. We use a flow-reaction model to explore how the interactions of sedimentary properties, fluid qualities, and reaction kinetics can lead to the current occurrence and distribution of GHs. We also focus on the growth and characteristics of fracture pathways in sediments within HSZ and how it propagates over GH content.

2. Geological Setting

The GMGS5 investigation area is located in the central channel of the upper slope of the QDN basin, adjacent to the Xisha Trough to the northeast (Figure 1b,c). Since the Neogene, the QDN basin has been in a post-rift thermal subsidence tectonic evolution stage. Wide-spreading Miocene (Huangliu formation), Pliocene (Yinggehai formation), and Quaternary (Ledong formation) marine sedimentary sequences formed in this period (Figure 1d). Since then, the local high deposition rate has led to the maximum sedimentary accumulation thickness along slope surface stretches about several kilometers [31–34]. The detrital sediments of the Holocene and Pleistocene age have a sand content of more than 50%. Elastoplastic unconsolidated argillaceous particles fill into skeleton matrixes. They serve as effective barriers to stop fluid from further smoothing upward seepage and provide sufficient space for GH storage. Previous exploration revealed that deep hydrocarbon source rocks developed below the Huangliu formation and have entered the mature hydrocarbon threshold. The thermal evolution degree of organic matter is in the range of a mature and high mature light oil and gas window, which has the geological conditions of forming thermogenic gas. Moreover, the strata above the Huangliu formation are within the formation condition of biogenic gas because most of the source rocks developed in the low mature–immature stage [35–38]. Intensive biogenic gas manifestation occur in petroleum drilling boreholes, especially those shallower than 2300 m below seafloor (mbsf). Both coal-measure mudstone (which generates thermogenic methane) and marine mud shale (which produces biogenic methane extensively) are potential source rocks here. The measured carbon isotope of methane is $-43.65\text{--}39.92\text{‰}$ the mixture origin of gas source [30].

A large number of gas chimneys are found in the study area, with a prevalent northeast direction. The acoustic blanking area is mushroom-shaped with the appearance status of a small lower part and a large upper part [24,39,40]. Most of these structures are firmly associated with the structures of faults and fractures [41]. Almost all gas chimneys here vertically extended from a T3 to T1 sequence, and their tops can be up to 200–150 mbsf gauging from two-way travel time [36]. Through characterizing the weak amplitude and chaotic seismic sections, three sets of MTD since the Late Quaternary have been confirmed above T1 interface, and laterally stretch across gas chimneys. With a high amplitude and reversed polarity, BSR here tends to sit above gas chimneys and just below the third MTD. Its wave impedance difference between the upper and lower layers is large and also shows a blank zone, indicating that probably abundant free gas is available within this study seabed [29,42].

3. Data and Methods

3.1. GHs in Site W08

The 2D seismic profile and instantaneous frequency profile collected in the GMGS5 expedition have been carefully inspected. From the characteristics of the BSRs, logging while drillings (LWDs), and lithologic coring results, the site W08 can be deemed as a representative well of this complex system because it is located exactly above the gas chimney section (Figure 2a,b). The deep seismic chimney is estimated to originate from 3 Ma BP. It is elliptic plane-shaped and has a diameter of several kilometers. The upward hydrocarbon fluids are reckoned to pass through this section and reach the T1 interface. The top of this seismic chimney shows the BSR occurrence and nearly coincides with the bottom of MTD3. A shallow fluid pipe shape in the seismic profile is observed, which has a

diameter of 180 m. It is columnar and calculated to be merely 0.5 Ma years old. This pipe is located just above the gas chimney area. Fluids will likely escape to the seafloor through it because the dome and pockmarks on the local seafloor that surface from remotely operated vehicle (ROV) observation indicate signs of fluid activity. Local high sedimentation rates since the early Pliocene easily trigger disequilibrium pore compression and bring about the overpressure outcome. In many situations, the fluid flow is mainly driven by the pore overpressure [24,40]. The lithology of the MTD3 here has a 20–50% clay content which is inferred to be older than 0.5 Ma BP. GHs in drilling core images mainly appear messy and discontinuous, and they grow in the fractures within MTD3. With strata stress and thermodynamic condition change, the performance of gas-driven hydraulic fracturing is presumed to occur extensively in this GH system.

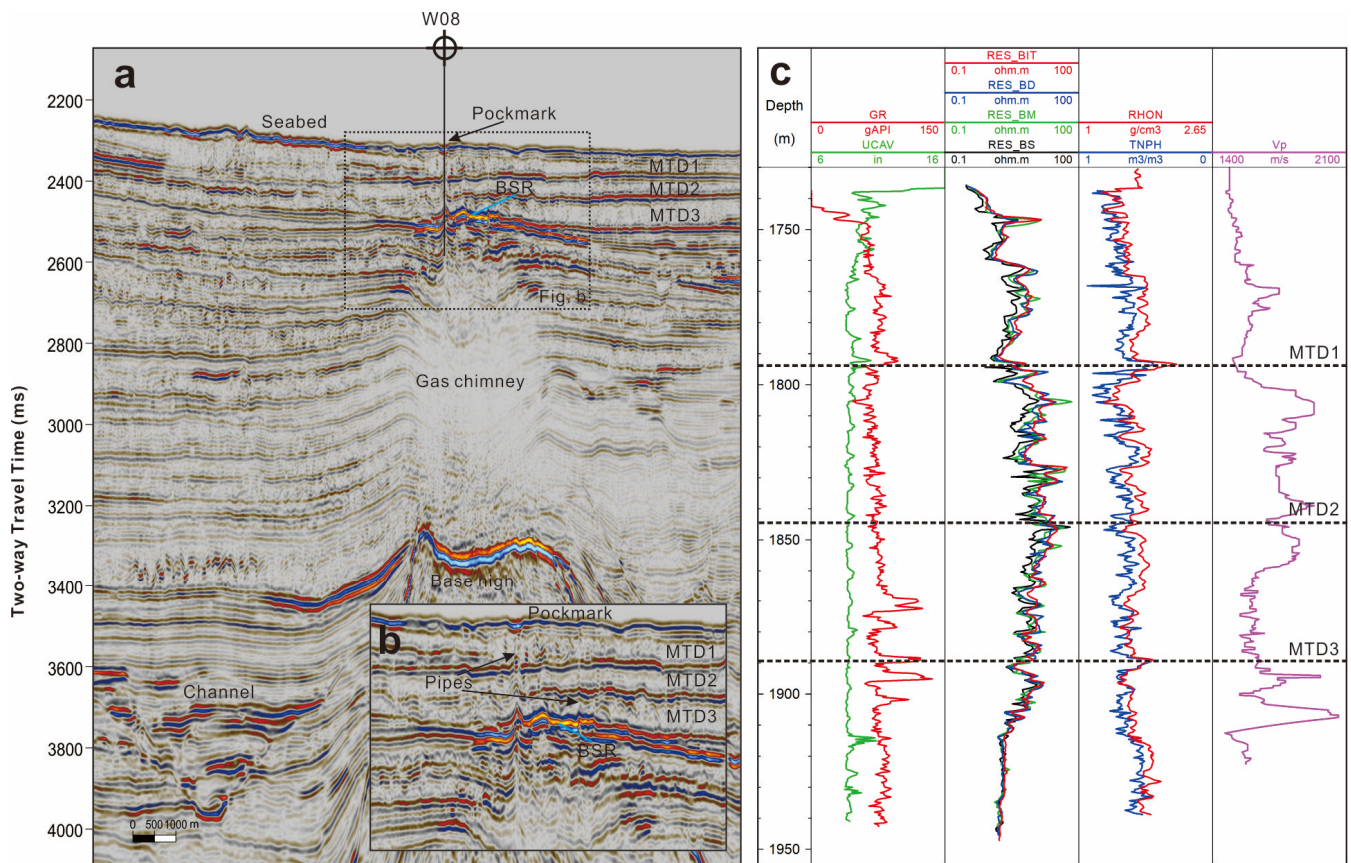


Figure 2. The structural configuration of site W08: (a) local seismic section, (b) zoomed seismic profile, and (c) three sets of MTD in LWD curves and their bottoms (MTD1-59, MTD2-112, and MTD3-157 mbsf).

3.2. Sea-Level Change and Deposition

The depth of seawater bottom in the GMGS5 investigation zone ranges from 1600 to 1800 m below sea level (mbsl). The deepest bottom boundary where GH core samples are drilled out is 237 mbsf. Nearly all GH layers occur above T1 interface (Figure 2b,c). The basin subsides since the Quaternary are roughly steady, and the sedimentary evolution is mainly controlled by the eustatic sea level change which is closely related to the Last Glacial Cycles that ended about 15,000 years ago. The detrital input is brought into the marginal sea by paleo-rivers [43]. Since seabed position changes can be calculated according to relative sea level and deposition rate v_{sed} (cm/kyr) (Figure 3a), the temperature and hydrostatic pressure at the bottom of the seawater are determined accordingly (Figure 3b). The recent rise in sea level in the area begins at about 30 kyr BP from historical inversion.

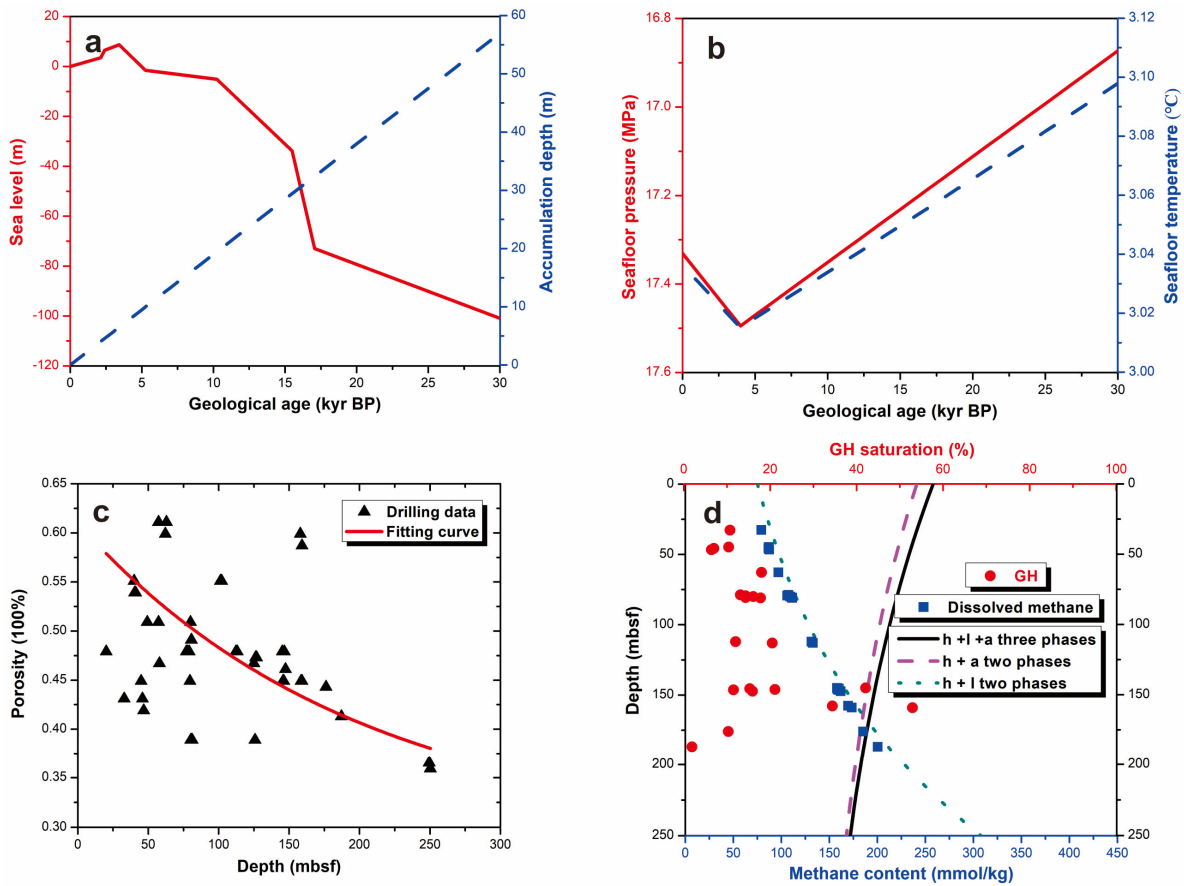


Figure 3. Local depositional conditions including: (a) sea level and sedimentation rate [44], (b) pressure and temperature change at seabed surface, (c) fitting on in situ porosity, and (d) methane concentration from drilling core test and phase lines in different situations (l-liquid, h-GH, and a-gas phase).

The distribution of deposit particle sizes and the skeleton in the seabed are often chaotic, and in particular, they suffer from the MTD influence. The measured local porosity distribution is plotted in Figure 3c. In order to simplify the treatment on the anomalous sedimentary layers, initial porosity ϕ_0 in deposits without GH existence is gauged by field data and its expression with depth z (mbsf):

$$\phi_0(z) = 0.29 + (\phi_{top} - 0.29) \times \exp(-0.00505z) \quad (R^2 = 0.2046), \quad (1)$$

where porosity at the sedimentary surface ϕ_{top} is 0.62. After GH forms in porous soil, we assume that the alteration of new porosity ϕ_h is suitable:

$$\phi_h(z) = \phi_0(z) \times (1 - S_h), \quad (2)$$

where S_h is GH saturation.

3.3. Methane in Pore Water

Through calculating the phase equilibrium curves of methane in liquid and gas states under local thermodynamic conditions [45–47], we compared how in situ GH is vertically distributed at GMGS5 site W08 (Figure 3d). It can be seen that methane supplies below HSZ bottom and even in the low part of HSZ are pretty abundant, so the current free gas is likely to be plentiful in these zones. We also inferred that maybe the GH reaction is still ongoing, while the methane gas in the middle and upper sections is completely converted into hydrates. The consequence is that merely GH and liquid water are preserved in local

pores. According to the data from degassing cores [29], the initial methane concentration n_{diss} (mmol/kg) in pores is quantified as:

$$n_{diss} = \exp(4.17 + 0.007 \times z - 5.18 \times 10^{-6} \times z^2). \tag{3}$$

3.4. Sedimentary Soil-Water Properties

We continue to adopt traditional normalized relating content to gauge sedimentary soil-water characteristics curves (SWCC), which is [48,49] as follows:

$$S_e = \frac{S_l + S_g - S_{li} - S_{gi}}{1 - S_{li} - S_{gi}}, \tag{4}$$

where S_e is effective fluid saturation; S_l and S_g are liquid and gas saturation, respectively; S_{li} and S_{gi} are initial irreducible liquid and gas saturation, and here S_{gi} is always 0. Irreducible liquid water S_{li} is considered to be controlled by clay content x_c and ϕ_h as [50]:

$$S_{li} = 0.326x_c^{0.219} + 0.0262/\phi_h. \tag{5}$$

The saturation-dependent relative permeability for gas k_{rg} and liquid k_{rl} phases can be defined by Corey’s model:

$$k_{rl} = (S_e)^{\frac{2+3\pi}{\pi}}, \tag{6}$$

and

$$k_{rg} = (1 - S_e)^2 \times [1 - (S_e)^{\frac{2+\pi}{\pi}}], \tag{7}$$

where the pore size profile exponent π is 7.3 in this simulation [51]. As the pressure difference between pore gas P_g (MPa) and liquid phases P_l (MPa), capillary pressure P_c (kPa) is defined by pore entry pressure P_{th} (kPa):

$$P_c = P_g - P_l = P_{th} \times S_e^{-1/\omega}, \tag{8}$$

where ω is another Brooks–Corey parameter. The demarcation on capillary drainage and the imbibition curves of shallow seabed sediments has been reasonably introduced by Daigle et al. (2020) [52] when tracing how gas-driven tensile fractures in marine hydrate-bearing layers. We use the same measurement to show the influence of clay fractions x_c , which are:

$$P_{th} = \exp[6.59(1 - \phi_h + S_{li})x_c - 2.76], \tag{9}$$

and

$$\omega = \exp(1.64x_c - 0.921). \tag{10}$$

The clay fraction scope in its seabed soil is 25–60%. When setting the layer porosity to be minimum 0.3 and maximum 0.7, the scope of the corresponding S_{li} ranges from 0.2781 to 0.3788.

3.5. Hydraulic Conductivity in Gas Chimney

Compared with the sedimentary transportation quality of fluids in other parts of northern SCS [53], we can use an exponential expression to depict the strata intrinsic permeability k_h (mD) after GH existence in the QDN area as:

$$k_h = k_0(1 - S_h)^3, \tag{11}$$

where k_0 (mD) is layer instinct permeability without GH existence. Based on the above description of the chimney–hydrate system, we set two different permeability values to reflect MTD influence. Within the 0–180 mbsf section, the permeability k_0 is reckoned as 2 mD. Below 180 mbsf, it is just within the gas chimney area and its value is 200 mD [30,36].

3.6. Tensile Strength Estimation

We also abide by the assumption that tensile failure can only occur when pore pressure steps across the resultant of minimum principle stress and the tensile strength of seabed soil together [52,54]. The final force difference criterion term S_v (MPa) in this work is:

$$S_v = P_c + P_l - T_{sp} - \sigma_h > 0. \tag{12}$$

The vertical stress σ_v (MPa) and horizontal stress σ_h (MPa) can be linked according to Poisson's ratio in the QDN area, and the expression is:

$$\frac{\sigma_h - P_l}{\sigma_v - P_l} = \frac{\nu}{1 - \nu} > 0.8. \tag{13}$$

The sub-seafloor σ_v is simplified as $\sigma_v = \rho_b g z$, and here the bulk sedimentary density ρ_b is 1910 kg/m³. The tensile strength T_{sp} (MPa) is determined as:

$$T_{sp} = -\frac{1}{2} \times 10^{[-6.36 + 2.45 \times \log_{10}(0.86 \times V_p - 1172)]} \times [m_i - \sqrt{m_i^2 + 4}], \tag{14}$$

where the Hoek–Brown constant m_i is 4, and compressional wave velocity V_p (m/s) at site W08 can be retrieved from the in situ logging curve as:

$$V_p = 2.47 \times z + 1470. \tag{15}$$

3.7. GH layer Formation Dynamics

From the comprehensive perspectives of gas source, kinetic reaction, fluid migration pathway, HSZ alteration, MTDs, and sedimentary soil properties, we established a one-dimensional dynamic evolution model, which is in line with the previous geological background, to demonstrate the accumulation process of hydrate-bearing sediments and put specific parsing steps and corresponding expressions in the Appendix A of this paper.

When the seawater depth is larger than 500 mbsl, the relationship of temperature at the seafloor surface T_{sf} (°C) with the depth L_w (mbsl) is [55]:

$$T_{sf} = \exp\{[2.0339 - \ln(L_w/1000)]/1.3361\} \tag{16}$$

The local temperature T_{se} (°C) in sediments is determined by geothermal gradient T_d (°C/m) and T_{sf} (°C), which is:

$$T_{se} = T_{sb} + z \times T_d. \tag{17}$$

All the parameter values in this basic simulation scene are listed in the following Table 1.

Table 1. Parameters used for deducing the basic scenario here.

Parameters	Values
Methane flux (kg·m ⁻² ·yr ⁻¹): q_m	0.25
Water flux (kg·m ⁻² ·yr ⁻¹): q_w	0
Geothermal heat (mW·yr ⁻²): q_e	80
Sedimentary rate (cm/kyr): v_s	19
Kinetic coefficient (mol·m ⁻³ ·MPa ⁻¹ ·yr ⁻¹): ζ_0	0.3
Total evolution time (kyr): t	30
Density (kg/m ³): $\rho_s, \rho_w, \rho_{g0}, \rho_h$	2650, 1025, 0.7 (standard temperature and pressure), 912
Molar mass (g/mol): η_w, η_m, η_h	18, 16, 124
Viscosity (Pa·s): μ_l, μ_g	$1.3 \times 10^{-3}, 1.5 \times 10^{-5}$
Diffusivity (m ² /s): D_1^m, D_1^s	$1.3 \times 10^{-9}, 1.0 \times 10^{-9}$
Initial salinity: X_{i0}^s	0.033
Fraction of clay particle volume: x_c	0.3
Geothermal gradient (°C/m): T_d	102
Heat conductivity (W·m ⁻¹ ·K ⁻¹): $\lambda_r, \lambda_l, \lambda_h, \lambda_g$	1.2, 0.58, 0.53, 0.05
Specific heat (J·kg ⁻¹ ·K ⁻¹): C_r, C_l, C_h, C_g	$2.2 \times 10^3, 4.2 \times 10^3, 2.1 \times 10^3, 3 \times 10^3$

4. Results

4.1. Evolution Process

The old seafloor depth at 30 kyr BP is calculated at 1790 mbsl in the light of the current sea level position. The earliest HSZ bottom boundary is 147 mbsf at that time. After the sedimentary process piles up, porewater pressure in accumulated sediments increases slightly to 0.0101 MPa/m, related to hydrostatic pressure 0.01 MP/m [56–58]. To better exhibit how this complex system consisting of a gas chimney, GH, pipe, and MTDs evolves, the following six key controlling factors, including strata pressure, temperature, capillary pressure, phase saturations, permeability, and salinity were chosen to represent system characteristics, as they can provide enough insightful strata information. Table 1 tells the basic thermodynamic and hydraulic environment about this complex GH system. Both the initial gas and hydrate content are 0 in this basic scene.

Five moments including four divided times (30, 20, 10, and 5 kyr BP), and the present, are selected to show the system evolution at that time. In Figure 4a, the positive pressure change is set as the difference between sedimentary pore pressure and seawater hydrostatic pressure if there is no deposition activity. Similarly, in Figure 4b, positive temperature change is defined as the difference between sedimentary temperature and seawater temperature if there are no sediments. Both of them verify the previous judgment that the depth of the local seafloor position increases from 30 to 5 kyr BP and then decreases a bit until now. GH is calculated to accumulate considerably within the lower part of HSZ and the maximum saturation of GH from model simulation can reach 47% (Figure 4c). It can be seen that both the GH distribution close to the HSZ bottom area and its peak of saturation coincide with the drilling data very well. Simulation results reveal that free gas will gradually gather at the top zone of the gas chimney, which is also the bottom zone of HSZ and MTD3. The current gas saturation is 20.3%, to possibly provoke BSR signs. Our results also demonstrate that GH and free gas can hardly coexist in pores, according to the strata setting of the gas chimney quality. The alternation of salinity and capillary pressure has a strong positive correlation with GH saturation, while permeability displays a wholly negative correlation (Figure 4d–f). These phenomena are consistent with the general cognition of marine GH sediments. Overall, the flow-reaction process, strata features, and the combination of related key parameter values perfectly explain how gas chimneys and MTD determine the dynamic evolution and final occurrence of GH systems.

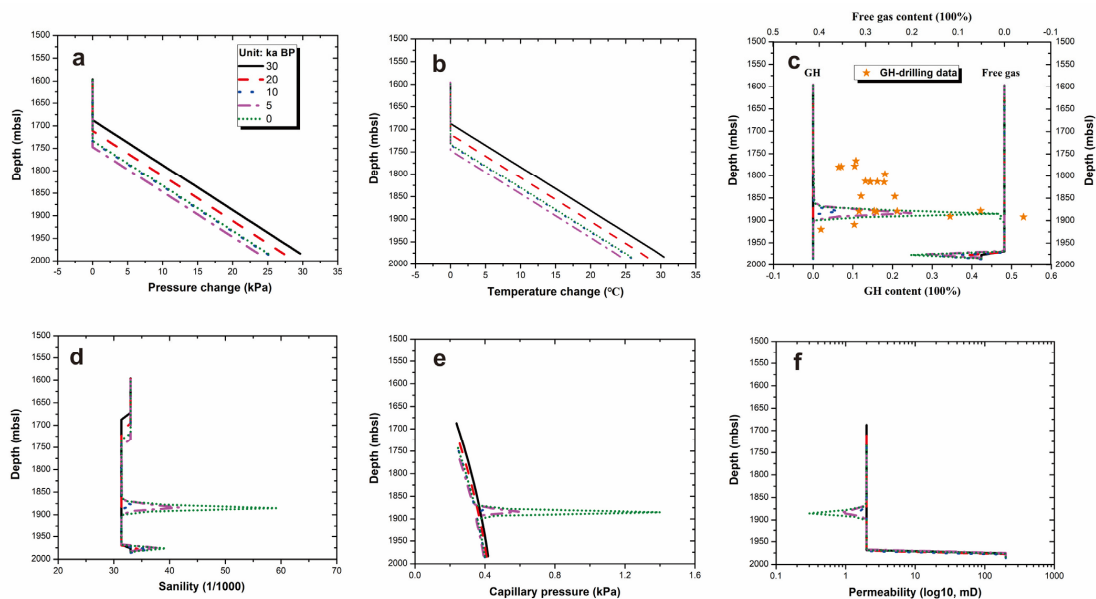


Figure 4. The evolution state of: (a) the change of pressure difference, (b) the change of temperature difference, (c) gas and hydrate content, (d) pore salinity, (e) capillary pressure, and (f) permeability, at five moments 30, 20, 10, 5 and 0 kyr BP.

4.2. Force Disequilibrium

The distribution of sedimentary stress and strength and corresponding force balance in this geological system attracted widespread attention in the academic community. Whether strata hydraulic fracturing occurs in clay-dominated fine-grained layers and how cracks are created by pore overpressure propagating in coarse-grained turbidities are essential to understanding GH existence and occurrence. Based on the stress and strength analysis in Equations (12)–(15), we calculated their values at these five moments in Figure 5a. The results show that the local tensile strength gradually decreases from the largest value at 30 kyr BP to the minimum at 5 kyr BP. After that, it increases rapidly. The current tensile strength is the same as that at 10 kyr BP. Meanwhile, the results of the criterion term, S_v , indicate that except for the bottom area of the studied strata at the beginning time of 30 kyr BP, the phenomenon of tensile fracture will always occur (Figure 5b). The strata are most likely to break at 5 kyr BP, and the existence of GH can greatly improve the possibility of fracturing behavior in the strata. GH saturation has an observably positive change with the term S_v .

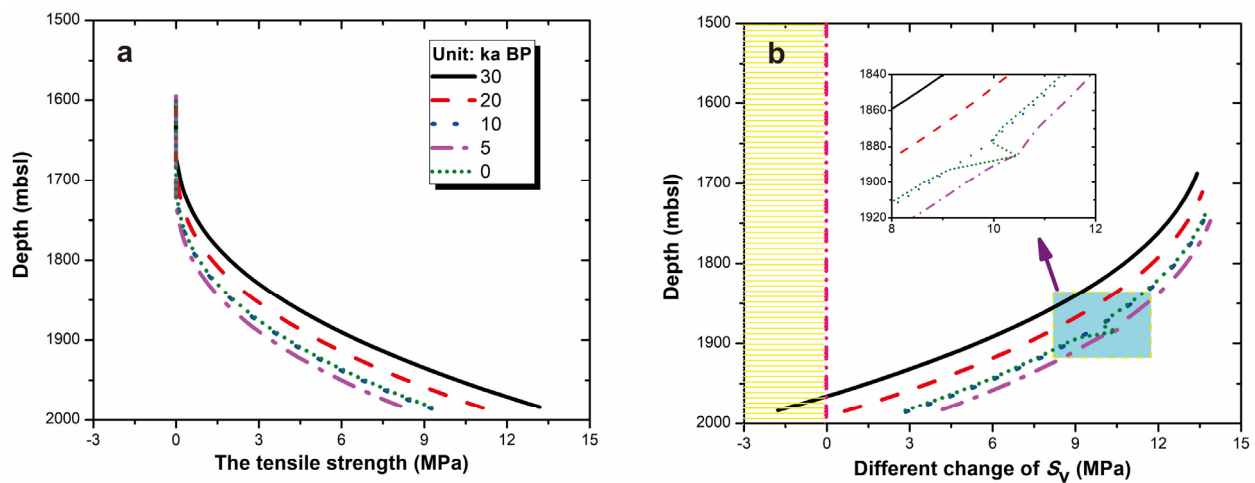


Figure 5. The evolution state of: (a) tensile strength, and (b) fracturing criterion term S_v at these five moments.

4.3. Different Sedimentary Conditions

Local gas supply, kinetic reaction, and permeability are three decisive variables in our model to simulate this GH system. We designed six other geological scenarios that can represent possible combinations of strata and fluid environments to cultivate diverse occurrences of hydrate-bearing sediments (Table 2). We presented the differences between the results of free gas, GH, and fracturing criterion term in these six scenarios and the previous basic condition (Figure 6a,b).

Table 2. Six possible geological scenarios for GH generation that may occur in the QDN area.

Scenarios	Gas Flux ($\text{kg}\cdot\text{m}^{-2}\cdot\text{yr}^{-1}$)	Kinetic Coefficient ($\text{mol}\cdot\text{m}^{-3}\cdot\text{MPa}^{-1}\cdot\text{yr}^{-1}$)	Permeability (in Chimney, in MTDs) (mD)
1	0.25	0.3	20,000, 2000
2	0.025	0.03	200, 2
3	2.5	0.03	200, 2
4	25	0.003	200, 20
5	250	0.03	200, 2
6	2500	0.03	2000, 2

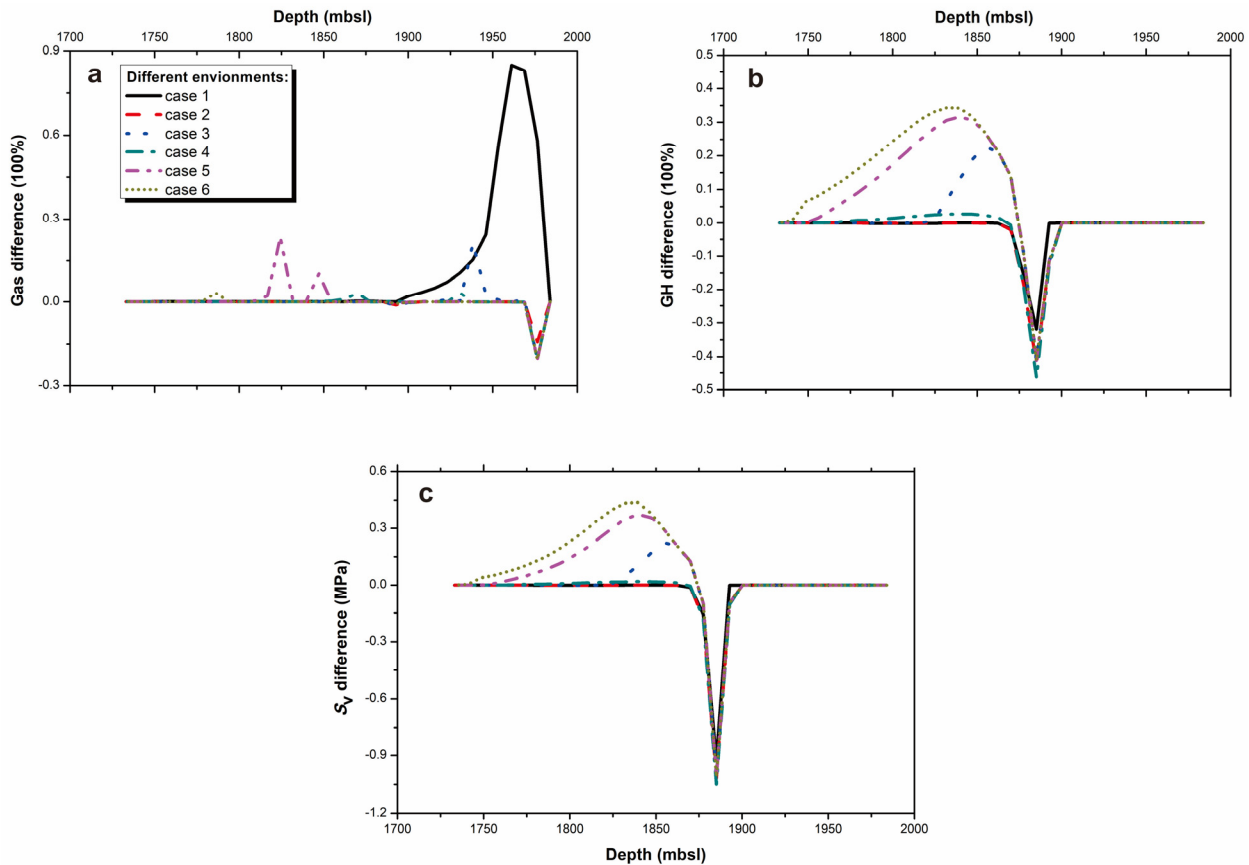


Figure 6. The differences of: (a) free gas, (b) GH, and (c) the criterion term S_v between the respective results of these six scenes and the previous basic condition.

Scenario 1 represents extremely high permeability in the gas chimney and the upper strata. The results show that the GH distribution range is nearly the same, but the saturation peak can only reach 15%. The gas peak can be up to 85%, and its distribution range is wider. GH and free gas can coexist in the HSZ. Scenario 2 shows less gas supply and kinetic reaction coefficient. The content of hydrates and free gas both decline dramatically. Scenario 3 shows a larger gas supply and a smaller reaction coefficient. The results indicate that the distribution of GH is wider. The highest position can reach about 95 mbsf, but the GH peak which shifts upward can only reach 23%. The free gas content is the same, but the peak position is also shifted higher. Scenario 4 represents a higher gas supply and the slowest reaction coefficient, while the upper sedimentary permeability increases. The results show that although the hydrate and free gas are more widely distributed, the contents of them are very low. Scenario 5 represents a higher gas supply and a slower kinetic reaction coefficient. The results show that although the hydrate distribution range is wide and the peak is high enough, there is also a wide range of free gas content in the HSZ with a peak value of 23%. Scenario 6 represents the largest gas supply, a smaller reaction coefficient, and a larger layer permeability in the gas chimney. GHs can fill the entire HSZ where sporadic free gas exists in the pores. By calculating these six fracturing criterion terms S_v , all the values are positive, indicating that fracturing will form or occur (Figure 6c). Meanwhile, the greater the hydrate content, the more likely that hydraulic fracturing will happen.

4.4. Palaeo-GH Existence

There is also a possibility that a certain amount of GH has already existed in the original HSZ before 30 kyr BP. With the rather big shift of the HSZ bottom boundary, the GH in the lower part decomposes until it vanishes, while the upper part remains there.

We set the three initial hydrate contents as 5% (case1), 10% (case2), and 15% (case3) to investigate the evolution process since 30 kyr BP. Similarly, we employ the difference of GH, free gas and fracturing criterion term S_v between these three cases and the corresponding value in the basic case. From the results, it can be seen that free gas contents also increase accordingly (Figure 7a). GH peaks at the HSZ bottom in the three cases can reach 53%, 57% and 59%, respectively. The possibility of a second peak is 9%, 19%, and 31% at about 105 mbsf where they nearly coincide with MTD2 bottom in Figure 7b. The criterion term curves are still positive, indicating that strata fracture will develop in these settings (Figure 7c). Furthermore, the higher the hydrate content, the more intensive the fracture behavior. On the whole, it is believed that the initial GH saturation of 10% is nearly perfect and more in line with the current observation about the GH existence close to MTD2 and MTD3 from drilling logging.

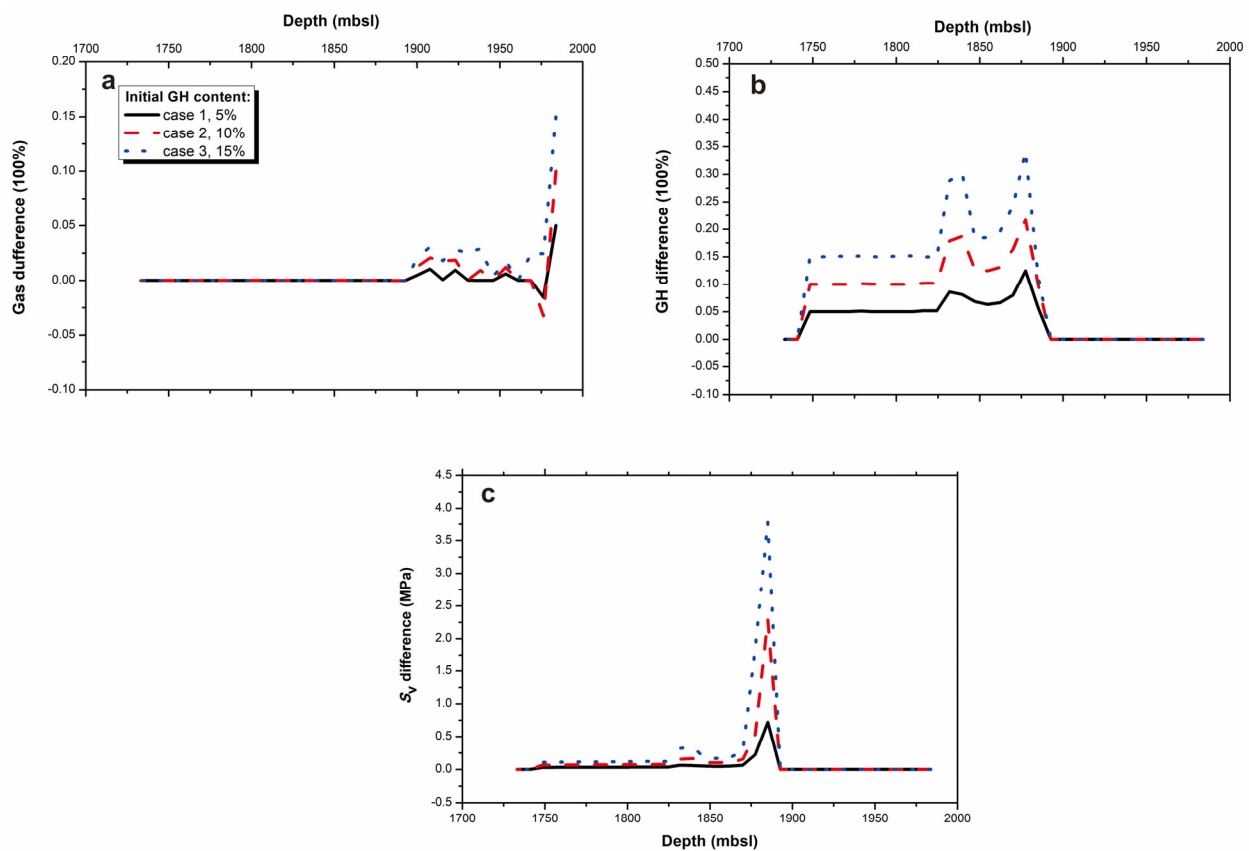


Figure 7. The difference of: (a) free gas, (b) GH, and (c) criterion term S_v with the corresponding value in the basic environment in three cases when initial GH saturation is 5%, 10%, and 15%, respectively.

5. Discussion

5.1. Petrophysical Variations

Except for the heterogeneity of sedimentary layers, other lithological variations of mixtures in the marine subsurface, including pore shape and connection, particle size distribution, and clay contents, exert strong impacts on fluid transport ability and the stiffness of skeleton endmembers. In our model, although the uniform lithology assumption is used to gauge this deposition-flow-reaction process, different values of the intrinsic permeability in separate gas chimneys and pipe zones have been set to roughly reflect the real lithological situation. One of the two uncertainties lies in the usage of the empirical parameters of SWCC properties in Equations (5)–(11). In our simulation, the general values of sedimentary factors are adopted, which define the drainage-imbibition performance of seabed soils. Another is the failure criterion to judge distinct Mohr–Coulomb hydraulic fracturing. We do not elaborate on the scopes of Poisson’s ratio, clay content, and the Hoek–Brown

constant here, because they are the mean values and can explain most ordinary cases in our research deposits.

5.2. Difference of MTDs

In our mode, we do not set any property discrepancies among the three MTDs. The simulation focus is on the lowest MTD3 because it almost marks both the bottom of HSZ and the top of BSR and dominates the unsaturated fluid flow qualities when passing into upper pipe space. Whether or not the overpressure created by upward fluids in gas chimneys gathering beneath MTD3 incites the pipe development via the hydraulic fracturing manner is still controversial. Undoubtedly, the latest emergence period of MTD2 and MTD3 is much earlier than 30 kyr BP because the calculated age of authigenic carbonate rocks at 52.1 mbsf is 0.53 Ma. The authigenic carbonate concretions lying along 3 mbsf level here are estimated to have formed at 3 kyr BP. The shallowest MTD1 is most likely to horizontally insert into the pipe structure. This activity impeded the upward fluid flow which just escaped from low MTD2 within the 30 kyr period. That is, multi-stage GH formation might have happened and led to the different occurrences of GHs among MTD1, MTD2, and MTD3 depth layers.

5.3. Multiple Accumulation Assumption

The analysis of paleo-GH existence suggests the great possibility that a multi-stage accumulation activity may have occurred. Rapid sedimentation together with sea level variations, landslides, and turbidity currents inevitably induces the simultaneous reaction of GH. The GH formation in the upper and middle layers of the sedimentary layer and decomposition in the lower part occurred [57,59]. Huge thick unconsolidated sedimentary seabed breeds and traps large amounts of methane-rich overpressure pore fluids. The mechanical disturbance in early MTD propagation easily triggered the internal rupture of the underlying muddy clay layer and prompted previously isolated pores to connect. The overpressure fluids subsequently penetrated the gas chimney channel, episodically migrated upward, and formed a hydrate-rich layer. After the MTD extension was completed, decreased permeability caused covered layers to serve as a sealing cap. These upward-migrating fluids were impeded. They had to gather largely at the bottom area of the MTDs and develop laterally. Local excellent GH resource sweet-spot layers with a certain thickness and depth were generated in this situation. This effect will be weakened with the temporal and spatial distribution sequence of the MTDs from bottom to top. From the difference in hydrate distribution at site W8, the oldest MTD3 has a GH abundance of up to 50%, and the second oldest MTD2 can also reach 20%. This phenomenon illustrates the rationality of our multiple accumulation speculations. Compared with other high-saturation hydrate reservoirs in oceanic hot reservoirs, such as the Alaminos Canyon in the Gulf of Mexico [60], Ulleung Basin, and the KG Basin offshore Kakinada, their drilling results are often firmly related to the MTD existence. Perhaps it provides a new point of view for hydrate resource exploration optimization.

6. Conclusions

The GH reservoirs firmly associated with gas chimney, pipe structure, and MTDs have been detected in GMGS5 investigation in the QDN area. How this gas chimney–hydrate geological system evolves and why GH-bearing sediments display the current distribution and occurrence attracts strong interest in probing its dynamic operation mechanism. Because site W08 shows representative system features, it is selected to elucidate the impact of environmental and geological factors, including sea-level change, sedimentation activity, soil-water qualities in and out of the gas chimney area, and MTDs on the evolution process. Through analyzing reasonable deposition-flow-reaction mode matching the local spatio-temporal geological background since 30 kyr BP, six key strata factors at five evolving moments are obtained. The sedimentary tensile fracture and occur at 5 kyr BP. Moreover, the evolution performance of this complex system in six other designed geological settings

is compared, and the possibility of three-content palaeo-GH occurrences before 30 kyr ago is discussed. Finally, we found that about 10% pre-existing GH seems to have the exact distribution and occurrence in fine-grained clayey silt layers adjacent to MTD2 and MTD3. However, how the overpressure created by gas-bearing fluid accumulating at the top of gas chimneys splits the overlying MTD strata and triggers the development of a large number of internal fractures within these layers has not yet been resolved.

Author Contributions: Conceptualization, J.G., W.Z. and M.H.; Data curation, M.W. and L.W.; Formal analysis, M.W., L.W. and Q.W.; Funding acquisition, J.G.; Investigation, L.W.; Methodology, J.G., W.Z., M.H. and Q.W.; Resources, W.Z. and M.H.; Supervision, M.H.; Validation, J.G. and M.H.; Visualization, Q.W.; Writing—original draft, J.G. and M.H.; Writing—review and editing, J.G., W.Z. and Q.W. All authors have read and agreed to the published version of the manuscript.

Funding: This work was jointly sponsored by the National Science Foundation of China (42176215), the Natural Science Foundation of Guangdong Province (2021A1515011515), China Scholarship Council (202104910252), the Guangzhou Science and Technology Planning Project (202201011434, 202201011409), the First Batch of the “Nanhai New Star” Project (NHXXRCXM202357), the Guangdong Basic and Applied Basic Research Foundation (2019B030302004), Project of Sanya Yazhou Bay Science and Technology City (SCKJ-JYRC-2023-02), Sanya Science and Technology Innovation Project (2022KJCX14), and Key-Area Research and Development Program of Guangdong Province (2023B1111050014).

Institutional Review Board Statement: Not applicable.

Informed Consent Statement: Not applicable.

Data Availability Statement: The source code used in this manuscript is written by Matlab language and can be downloaded at an open-source online data repository (accessed on 12 March 2024, <https://data.mendeley.com/datasets/vtkgd4zgsx>; doi:10.17632/vtkgd4zgsx.1). Figures 4–6 were obtained from simulation data using this code and drawn with OriginPro 2016. The codes in this article are permitted for noncommercial or academic use, sharing, adaptation, distribution, and reproduction, and credit to the original authors is appreciated.

Acknowledgments: We would like to thank for the support and suggestions from Elke Kossel, and Christian Deusner throughout the whole research process.

Conflicts of Interest: The authors declare no conflicts of interest.

Appendix A. A Flow-Reaction Model

We conceived this gas chimney–hydrate compound geological system as a multi-phase transportation process in porous sediments, which includes three phases (h, l and a) and four components (h, water-w, methane-m, and salt-s). Firstly, GH kinetic reaction r_h ($\text{mol}\cdot\text{m}^{-3}\cdot\text{yr}^{-1}$) can be expressed as the gradient difference consequence of the fugacity under the local thermodynamic condition f (MPa) and equilibrium condition f_{eq} (MPa), respectively:

$$r_h = \zeta_0 \exp\left[-\frac{\Delta E_a}{R}\left(\frac{1}{T_{se}} - \frac{1}{T_{eq}}\right)\right] \phi_h (f - f_{eq}), \quad (\text{A1})$$

where ζ_0 ($\text{mol}\cdot\text{m}^{-3}\cdot\text{MPa}^{-1}\cdot\text{yr}^{-1}$) is the kinetic coefficient of GH reaction; $\Delta E_a/R$ is 9752.73 K; T_{eq} (K) is the equilibrium temperature. The corresponding water r_w ($\text{mol}\cdot\text{m}^{-3}\cdot\text{yr}^{-1}$) and methane r_m ($\text{mol}\cdot\text{m}^{-3}\cdot\text{yr}^{-1}$) have the following relations:

$$r_w = 5.76 \times r_h, \quad (\text{A2})$$

and

$$r_m = r_h. \quad (\text{A3})$$

It is assumed that methane is immersed into pore gas and liquid, as follows:

$$\begin{aligned} & \frac{\partial}{\partial t} [\phi(\rho_g S_g + \rho_l S_l X_l^m)] + \nabla \cdot \left[\begin{array}{l} -\rho_g k_h \frac{k_{rg}}{\mu_g} (\nabla P_g - \rho_g g) \\ -\rho_l k_h \frac{k_{rl}}{\mu_l} (\nabla P_l - \rho_l g) X_l^m - \phi \rho_l D_l^m \nabla X_l^m \end{array} \right] \\ & = -\eta_m r_m + \nabla \cdot q_m \end{aligned} \quad (A4)$$

Similar to the water component, we have:

$$\frac{\partial}{\partial t} [\phi \rho_l S_l X_l^w] + \nabla \cdot \left[-\rho_l k_h \frac{k_{rl}}{\mu_l} (\nabla P_l - \rho_l g) X_l^w \right] = -\eta_w r_w + \nabla \cdot q_w. \quad (A5)$$

The current salinity X_l^s is merely defined by initial liquid saturation S_{l0} and initial salinity X_{l0}^s :

$$X_l^s = \frac{S_{l0}}{S_l} X_{l0}^s. \quad (A6)$$

The expression of GH is as follows:

$$\frac{\partial}{\partial t} (\phi S_h \rho_h) = \eta_h r_h. \quad (A7)$$

In the above equations, ρ_κ (kg/m^3) ($\kappa = a, l, h$) is the phase density; X_l^m , X_l^w , and X_l^s are the mass fractions of methane, water, and salt in pore water; η_i is mole mass ($i = m, w, h$); μ_κ ($\text{Pa}\cdot\text{s}$) ($\kappa = a, l$) is phase viscosity; g is $9.8 \text{ N}/\text{kg}$; t (yr) is time; D_l^m and D_l^s (m^2/s) are diffusion coefficients of methane and salt in liquids; q_i ($\text{kg}\cdot\text{m}^{-2}\cdot\text{yr}^{-1}$) is component flux ($i = m, w$).

The total heat energy balance is:

$$\begin{aligned} & [(1 - \phi_h) \rho_r C_r + \phi_h (\rho_h C_h S_h + \rho_l C_l S_l + \rho_g C_g S_g)] \frac{\partial T_{se}}{\partial t} + [C_g \rho_g u_g + C_l \rho_l u_l] \frac{\partial T_{se}}{\partial z} \\ & = \frac{\partial}{\partial z} \left\{ [(1 - \phi_h) \lambda_r + \phi_h (S_h \lambda_h + S_g \lambda_g + S_l \lambda_l)] \frac{\partial T_{se}}{\partial z} \right\} + Q_h + \nabla \cdot q_e \end{aligned} \quad (A8)$$

where C_κ ($\text{J}\cdot\text{kg}^{-1}\cdot\text{K}^{-1}$) and λ_κ ($\text{W}\cdot\text{m}^{-1}\cdot\text{K}^{-1}$) ($\kappa = r, h, l$, and a) are phase-specific heat and heat conductivity, respectively; q_e is local heat flow (mW/m^2). Darcy velocity of phases u_κ ($\kappa = l, a$) are:

$$u_g = -k_h \frac{k_{rg}}{\mu_g} (\nabla P_g - \rho_g g), \quad (A9)$$

and

$$u_l = -k_h \frac{k_{rl}}{\mu_l} (\nabla P_l - \rho_l g). \quad (A10)$$

Finally, the latent heat of GH in reaction Q_h ($\text{J}\cdot\text{m}^{-3}\cdot\text{s}^{-1}$) is:

$$Q_h = \eta_h r_h \times (446.12 \times 10^3 - 132.638 \times T_{se}). \quad (A11)$$

References

- Collett, T.; Bahk, J.; Baker, R.; Boswell, R.; Divins, D.; Frye, M.; Goldberg, D.; Husebø, J.; Koh, C.; Malone, M.; et al. Methane hydrates in nature—Current knowledge and challenges. *J. Chem. Eng. Data* **2015**, *60*, 319–329. [\[CrossRef\]](#)
- Boswell, R.; Shipp, C.; Reichel, T.; Shelander, D.; Saeki, T.; Frye, M.; Shedd, W.; Collett, T.S.; McConnell, D.R. Prospecting for marine gas hydrate resources. *Interpretation* **2016**, *4*, SA13–SA24. [\[CrossRef\]](#)
- Cook, A.E.; Portnov, A.; Heber, R.C.; Vadakkepuliambatta, S.; Bunz, S. Widespread subseafloor gas hydrate in the Barents Sea and Norwegian Margin. *Earth Planet. Sci. Lett.* **2023**, *604*, 117993. [\[CrossRef\]](#)
- Liu, J.; Haeckel, M.; Rutqvist, J.; Wang, S.; Yan, W. The mechanism of methane gas migration through the gas hydrate stability zone: Insights from numerical simulations. *JGR Solid Earth* **2019**, *124*, 4399–4427. [\[CrossRef\]](#)
- Bello, A.; Heggland, R.; Peacock, D.C.P. Pressure significance of gas chimneys. *Mar. Pet. Geol.* **2017**, *86*, 402–407. [\[CrossRef\]](#)
- Elger, J.; Berndt, C.; Rupke, L.; Krastel, S.; Gross, F.; Geissler, W.H. Submarine slope failures due to pipe structure formation. *Nat. Commun.* **2018**, *9*, 715. [\[CrossRef\]](#) [\[PubMed\]](#)

7. Robinson, A.H.; Callow, B.; Bottner, C.; Yilo, N.; Provenzano, G.; Falcon-Suarez, I.H.; Marin-Moreno, H.; Lichtschlag, A.; Bayrakci, G.; Gehrmann, R.; et al. Multiscale characterization of chimneys/pipes: Fluid escape structures within sedimentary basins. *International J. Greenh. Gas Control* **2021**, *106*, 103245. [[CrossRef](#)]
8. Dentzer, J.; Bruel, D.; Delescluse, M.; Chamot-Rooke, N.; Beccaletto, L.; Lopez, S.; Courrioux, G.; Violette, S. Thermal and seismic hints for chimney type cross-stratal fluid flow in onshore basins. *Sci. Rep.* **2018**, *8*, 15330. [[CrossRef](#)]
9. Han, W.; Chen, L.; Liu, C. Distribution and characteristics of gas chimneys in the passive margin offshore SW Taiwan. *Mar. Geophys. Res.* **2021**, *42*, 25. [[CrossRef](#)]
10. Hovland, M.; Sommerville, J.H. Characteristics of two natural gas seepages in the North Sea. *Mar. Pet. Geol.* **1985**, *2*, 319–326. [[CrossRef](#)]
11. Hovland, M. The formation of pockmarks and their potential influence on offshore construction. *Q. J. Eng. Geol. Hydrogeol.* **1989**, *22*, 131–138. [[CrossRef](#)]
12. Hovland, M.; Svensen, H. Submarine pingoes: Indicators of shallow gas hydrates in a pockmark at Nyegga, Norwegian Sea. *Mar. Geol.* **2006**, *228*, 15–23. [[CrossRef](#)]
13. Cheng, C.; Jiang, T.; Kuang, Z.; Ren, J.; Liang, J.; Lai, H.; Xiong, P. Seismic characteristics and distributions of Quaternary mass transport deposits in the Qiongdongnan Basin, northern South China Sea. *Mar. Pet. Geol.* **2021**, *129*, 105118. [[CrossRef](#)]
14. Yang, J.; Davies, R.J.; Huuse, M. Gas migration below gas hydrates controlled by mass transport complexes, offshore Mauritania. *Mar. Pet. Geol.* **2013**, *48*, 366–378. [[CrossRef](#)]
15. Chatterjee, S.; Bhatnagar, G.; Dugan, B.; Dickens, G.R.; Chapman, W.G.; Hirasaki, G.J. The impact of lithologic heterogeneity and focused fluid flow upon gas hydrate distribution in marine sediment. *J. Geophys. Res. Solid Earth* **2014**, *119*, 6705–6732. [[CrossRef](#)]
16. Guan, J.; Wan, L.; Liang, D. Gauging formation dynamics of structural-seepage methane hydrate reservoirs in Shenhu area of northern South China Sea: Impact of seafloor sedimentation and assessment of controlling factors. *Mar. Pet. Geol.* **2019**, *107*, 185–197. [[CrossRef](#)]
17. Yang, S.; Liang, J.; Lu, J.; Qu, C.; Liu, B. New understandings on characteristic and controlling factors of gas hydrate reservoirs in Shenhu area on northern slope of South China Sea. *Earth Sci. Front.* **2017**, *24*, 1–14, (In Chinese with English abstract).
18. Cathles, L.M.; Su, Z.; Chen, D. The physics of gas chimney and pockmark formation, with implications for assessment of seafloor hazards and gas sequestration. *Mar. Pet. Geol.* **2010**, *27*, 82–91. [[CrossRef](#)]
19. Sun, Q.; Cartwright, J.; Wu, S.; Chen, D. 3D seismic interpretation of dissolution pipes in the South China Sea: Genesis by subsurface, fluid induced collapse. *Mar. Geol.* **2013**, *337*, 171–181. [[CrossRef](#)]
20. Wan, Z.; Zhang, W.; Ma, C.; Liang, J.; Li, A.; Meng, D.; Huang, W.; Yang, C.; Zhang, J.; Sun, Y. Dissociation of gas hydrates by hydrocarbon migration and accumulation-derived slope failures: An example from the South China Sea. *Geosci. Front.* **2021**, *12*, 101345. [[CrossRef](#)]
21. Argentino, C.; Conti, S.; Fioroni, C.; Fontana, D. Evidences for Paleo-Gas Hydrate Occurrence: What We Can Infer for the Miocene of the Northern Apennines (Italy). *Geosciences* **2019**, *9*, 134. [[CrossRef](#)]
22. Chun, J.H.; Bahk, J.J.; Um, I.K. Ulleung basin gas hydrate drilling expeditions, Korea: Lithologic characteristics of gas hydrate-bearing sediments. In *World Atlas of Submarine Gas Hydrates in Continental Margins*; Mienert, J., Berndt, C., Tréhu, A.M., Camerlenghi, A., Liu, C.S., Eds.; Springer: Cham, Switzerland, 2022; pp. 155–161.
23. Collett, T.S.; Chopra, K.; Bhardwaj, A.; Boswell, R.; Waite, W.F.; Misra, A.K.; Kumar, P. A review of the exploration, discovery and characterization of highly concentrated gas hydrate accumulations in coarse-grained reservoir systems along the eastern continental margin of India. In *World Atlas of Submarine Gas Hydrates in Continental Margins*; Mienert, J., Berndt, C., Tréhu, A.M., Camerlenghi, A., Liu, C.S., Eds.; Springer: Cham, Switzerland, 2022; pp. 139–154.
24. Liang, C.; Liu, C.; Xie, X.; Yu, X.; He, Y.; Su, M.; Chen, H.; Zhou, Z.; Tian, D.; Mi, H.; et al. Basal shear zones of recurrent mass transport deposits serve as potential reservoirs for gas hydrates in the Central Canyon area, South China Sea. *Mar. Geol.* **2021**, *441*, 106631. [[CrossRef](#)]
25. Zhao, Z.; Sun, Z.; Wan, Z.; Liu, J.; Zhang, C. The high resolution sedimentary filling in Qiongdongnan Basin, northern South China Sea. *Mar. Geol.* **2015**, *361*, 11–24. [[CrossRef](#)]
26. Zhao, Z.; Sun, Z.; Sun, L.; Wang, Z.; Sun, Z. Cenozoic tectonic subsidence in the Qiongdongnan Basin, northern South China Sea. *Basin Res.* **2018**, *30* (Suppl. S1), 269–288. [[CrossRef](#)]
27. Deng, W.; Liang, J.; Zhang, W.; Kuang, Z.; Zhong, T.; He, Y. Typical characteristics of fracture-filling hydrate-charged reservoirs caused by heterogeneous fluid flow in the Qiongdongnan Basin, northern South China Sea. *Mar. Pet. Geol.* **2021**, *124*, 104810.
28. Lai, H.; Fang, Y.; Kuang, Z.; Ren, J.; Liang, J.; Lu, J.; Wang, G.; Xing, C. Geochemistry, origin and accumulation of natural gas hydrates in the Qiongdongnan Basin, South China Sea: Implications from site GMGS5-W08. *Mar. Pet. Geol.* **2021**, *123*, 104774. [[CrossRef](#)]
29. Wei, J.; Liang, J.; Lu, J.; Zhang, W.; He, Y. Characteristics and dynamics of gas hydrate systems in the northwestern South China Sea—Results of the fifth gas hydrate drilling expedition. *Mar. Pet. Geol.* **2019**, *110*, 287–298. [[CrossRef](#)]
30. Ye, J.; Wei, J.; Liang, J.; Lu, J.; Lu, H.; Zhang, W.; all the participants of GMGS5. Complex gas hydrate system in a gas chimney, South China Sea. *Mar. Pet. Geol.* **2019**, *104*, 29–39. [[CrossRef](#)]
31. Gong, C.; Wang, Y.; Zhu, W.; Li, W.; Xu, Q.; Zhang, J. The central submarine canyon in the Qiongdongnan Basin, northwestern South China Sea: Architecture, sequence stratigraphy, and depositional processes. *Mar. Pet. Geol.* **2011**, *28*, 1690–1702. [[CrossRef](#)]

32. Li, W.; Alves, T.M.; Wu, S.; Volker, D.; Zhao, F.; Mi, L.; Kopf, A. Recurrent slope failure and submarine channel incision as key factors controlling reservoir potential in the South China Sea (Qiongdongnan Basin, South Hainan Island). *Mar. Pet. Geol.* **2015**, *64*, 17–30. [[CrossRef](#)]
33. Ren, J.; Cheng, C.; Xiong, P.; Kuang, Z.; Liang, J.; Lai, H.; Chen, Z.; Chen, Y.; Li, T.; Jiang, T. Sand-rich gas hydrate and shallow gas systems in the Qiongdongnan Basin, northern South China Sea. *J. Pet. Sci. Eng.* **2022**, *215 Pt B*, 110630. [[CrossRef](#)]
34. Wang, Z.; Jiang, T.; Zhang, D.; Wang, Y.; Zuo, Q.; He, W. Evolution of deepwater sedimentary environments and its implication for hydrocarbon exploration in Qiongdongnan Basin, northwestern South China Sea. *Acta Oceanol. Sin.* **2015**, *34*, 1–10. [[CrossRef](#)]
35. Huang, B.; Tian, H.; Li, X.; Wang, Z.; Xiao, X. Geochemistry, origin and accumulation of natural gases in the Deepwater area of the Qiongdongnan Basin, South China Sea. *Mar. Pet. Geol.* **2016**, *72*, 254–267. [[CrossRef](#)]
36. Liang, J.; Zhang, W.; Lu, J.; Wei, J.; Kuang, Z.; He, Y.; all participants of GMGS5 expedition. Geological occurrence and accumulation mechanism of natural gas hydrates in the eastern Qiongdongnan Basin of the South China Sea: Insights from site GMGS5-W9-2018. *Mar. Pet. Geol.* **2019**, *418*, 106042. [[CrossRef](#)]
37. Meng, M.; Liang, J.; Lu, J.; Zhang, W.; Kuang, Z.; Fang, Y.; He, Y.; Deng, W.; Huang, W. Quaternary deep-water sedimentary characteristics and their relationship with the gas hydrate accumulations in the Qiongdongnan Basin, Northwest South China Sea. *Deep-Sea Res.* **2021**, *177*, 103628. [[CrossRef](#)]
38. Zhang, W.; Liang, J.; Yang, X.; Su, P.; Wan, Z. The formation mechanism of mud diapirs and gas chimneys and their relationship with natural gas hydrates: Insights from the deep-water area of Qiongdongnan Basin, northern South China Sea. *Int. Geol. Rev.* **2018**, *62*, 789–810. [[CrossRef](#)]
39. Zhang, W.; Liang, J.; Zhang, R.; Deng, W.; Gu, Y.; He, Y.; Gong, Y.; Meng, M.; Feng, J.; Liang, J. Gas hydrate accumulation in shelf break setting: Example from the Qiongdongnan Basin in the northern slope of the South China Sea. *Geol. J.* **2022**, *57*, 1153–1171. [[CrossRef](#)]
40. Yang, W.; Kuang, Z.; Ren, J.; Liang, J.; Lu, H.; Ning, Z.; Xu, C.; Lai, H.; Chen, R.; Zhao, B.; et al. The controlling factors of the natural gas hydrate accumulation in the Songnan Low Uplift, Qiongdongnan Basin, China. *Front. Earth Sci.* **2022**, *10*, 882080.
41. Conti, S.; Fontana, D.; Lucente, C.C.; Pini, G.A. Relationships between seep-carbonates, mud volcanism and basin geometry in the Late Miocene of the northern Apennines of Italy: The Montardone mélange. *Int. J. Earth Sci. (Geol. Rundsch.)* **2014**, *103*, 281–295. [[CrossRef](#)]
42. Liu, S.; Feng, X.; Feng, Z.; Xiao, X.; Feng, L. Geochemical evidence of methane seepage in the sediments of the Qiongdongnan Basin, South China Sea. *Chem. Geol.* **2020**, *543*, 119588. [[CrossRef](#)]
43. He, Y.; Liang, J.; Kuang, Z.; Deng, W.; Ren, J.; Lai, H.; Meng, M.; Zhang, W. Migration and accumulation characteristics of natural gas hydrates in the uplifts and their slope zones in the Qiongdongnan Basin, China. *China Geol.* **2022**, *5*, 234–250. [[CrossRef](#)]
44. Deng, Y.; Chen, F.; Guo, Q.; Hu, Y.; Chen, D.; Yang, S.; Cao, J.; Chen, H.; Wei, R.; Cheng, S.; et al. Possible links between methane seepages and glacial-interglacial transitions in the South China Sea. *Geophys. Res. Lett.* **2021**, *48*, e2020GL091429. [[CrossRef](#)]
45. Davie, M.K.; Zatsepina, O.Y.; Buffett, B.A. Methane solubility in marine hydrate environments. *Mar. Geol.* **2004**, *203*, 177–184. [[CrossRef](#)]
46. Duan, Z.; Moller, N.; Greenberg, J.; Weare, J. The prediction of methane solubility in natural waters to high ionic strength from 0 to 250 °C and from 0 to 1600 bar. *Geochim. Cosmochim. Acta* **1992**, *56*, 1451–1460. [[CrossRef](#)]
47. Tishchenko, P.; Hensen, C.; Wallmann, K.; Wong, C.S. Calculation of the stability and solubility of methane hydrate in seawater. *Chem. Geol.* **2005**, *219*, 37–52. [[CrossRef](#)]
48. Fredlund, D.G.; Xing, A.; Huang, S. Predicting the permeability function for unsaturated soils using the soil-water characteristic curve. *Can. Geotech. J.* **1994**, *31*, 533–546. [[CrossRef](#)]
49. Murphy, Z.W.; DiCarlo, D.A.; Flemings, P.B.; Daigle, H. Hydrate is a nonwetting phase in porous media. *Geophys. Res. Lett.* **2020**, *47*, e2020GL089289. [[CrossRef](#)]
50. Daigle, H.; Ghanbarian, B.; Henry, P.; Conin, M. Universal scaling of the formation factor in clays: Example from the Nankai Trough. *J. Geophys. Res. Solid Earth* **2015**, *120*, 7361–7375. [[CrossRef](#)]
51. Guan, J.; Liang, D.; Wu, N.; Fan, S. The methane hydrate formation and the resource estimate resulting from free gas migration in seeping seafloor hydrate stability zone. *J. Asian Earth Sci.* **2009**, *36*, 277–288. [[CrossRef](#)]
52. Daigle, H.; Cook, A.; Fang, Y.; Bihani, A.; Song, W.; Flemings, P.B. Gas-driven tensile fracturing in shallow marine sediments. *JGR Solid Earth* **2020**, *125*, e2020JB020835. [[CrossRef](#)]
53. Wei, J.; Yang, L.; Liang, Q.; Liang, J.; Lu, J.; Zhang, W.; Zhang, X.; Lu, X. Geomechanical properties of gas hydrate-bearing sediments in Shenhu Area of the South China Sea. *Energy Rep.* **2021**, *7*, 8013–8020. [[CrossRef](#)]
54. Crutchley, G.J.; Mountjoy, J.J.; Hillman, J.I.T.; Turco, F.; Watson, S.; Flemings, P.B.; Davy, B.; Woelz, S.; Gorman, A.R.; Bialas, J. Upward-Doming Zones of Gas Hydrate and Free Gas at the Bases of Gas Chimneys, New Zealand’s Hikurangi Margin. *JGR Solid Earth* **2021**, *126*, e2020JB021489. [[CrossRef](#)]
55. Su, P.; Liang, J.; Peng, J.; Zhang, W.; Xu, Z. Petroleum systems modeling on gas hydrate of the first experimental exploitation region in the Shenhu area, northern South China Sea. *J. Asian Earth Sci.* **2018**, *16*, 57–76. [[CrossRef](#)]
56. Bi, G.; Lyu, C.; Li, C.; Chen, G.; Zhang, G.; Zhou, Q.; Li, C.; Zhao, Y. Impact of early hydrocarbon charge on the diagenetic history and reservoir quality of the Central Canyon sandstones in the Qiongdongnan Basin, South China Sea. *J. Asian Earth Sci.* **2019**, *185*, 104022. [[CrossRef](#)]

57. Guan, J.; Liang, Y.; Wang, S.; Wan, L.; Fan, S.; Su, P.; Zhang, W.; Liang, D. New insight on the stratigraphic-diffusive gas hydrate system since the Pleistocene in the Dongsha area of the Northeastern South China Sea. *J. Mar. Sci. Eng.* **2022**, *10*, 434. [[CrossRef](#)]
58. Riboulot, R.; Cattaneo, A.; Sultan, N.; Ker, S.G.; Imbert, P.; Voisset, M. Sea-level change and free gas occurrence influencing a submarine landslide and pockmark formation and distribution in deepwater Nigeria. *Earth Planet. Sci. Lett.* **2013**, *375*, 78–91. [[CrossRef](#)]
59. Wang, B.; Lei, H.; Huang, F.; Kong, Y.; Pan, F.; Cheng, W.; Chen, L.; Guo, L. Effect of Sea-Level Change on Deep-Sea Sedimentary Records in the Northeastern South China Sea over the past 42 kyr. *Geofluids* **2020**, *2020*, 8814545. [[CrossRef](#)]
60. Boswell, R.; Collett, T.S.; Frye, M.; Shedd, W.; McConnell, D.R.; Shelander, D. Subsurface gas hydrates in the northern Gulf of Mexico. *Mar. Pet. Geol.* **2012**, *34*, 4–30. [[CrossRef](#)]

Disclaimer/Publisher’s Note: The statements, opinions and data contained in all publications are solely those of the individual author(s) and contributor(s) and not of MDPI and/or the editor(s). MDPI and/or the editor(s) disclaim responsibility for any injury to people or property resulting from any ideas, methods, instructions or products referred to in the content.